Microstructure and oxidation behavior of the CrMoNbTaV high-entropy alloy

Yifeng Xiao, Wenhui Kuang, Yanfei Xu,[a] Liang Wu, Wenjuan Gong, Jinwen Qian, and Qiankun Zhang
School of Mechanical Engineering, Xiangtan University, Xiangtan 411105, People's Republic of China; Key Laboratory of Welding Robot and Application Technology of Hunan Province, Xiangtan University, Xiangtan 411105, People's Republic of China; and Engineering Research Center of Complex Tracks Processing Technology and Equipment of Ministry of Education, Xiangtan University, Xiangtan 411105, People's Republic of China

Yuehui He
State Key Laboratory of Powder Metallurgy, Central South University, Changsha 410083, People's Republic of China

(Received 13 June 2018; accepted 21 August 2018)

The microstructure and oxidation behavior at high temperatures ranging from 900 °C to 1100 °C of equiatomic CrMoNbTaV high-entropy alloy produced by vacuum arc melting were investigated. The phase component, microstructure, and microhardness of the alloy were examined by using X-ray diffraction, scanning electron microscopy equipped with an energy-dispersive X-ray spectroscope, and Vickers hardness tests, respectively. The as-cast alloy consists of a single body-centered cubic (BCC) refractory metal solid solution due to the high mixing entropy effect and exhibits a dendritic microstructure. The alloy has a very high microhardness value of 923 HV due to the strong solid solution strengthening effect. The average microhardness in interdendrites (950 HV) was higher than that in dendrites (896 HV) because of composition segregation. The oxidation kinetic curves of the alloy after exposure to air at 900 and 1000 °C follow the pseudo-parabolic rate law, while the mass gain increases first and then decreases at 1100 °C. The thickness of the oxide layer increases with the increasing of oxidation time. The long rod-shaped oxidation products are composed of Nb_2O_5, NbO_2, $CrTaO_4$, $CrNbO_4$, Ta_9VO_{25}, Nb_9VO_{25}, and TaO after oxidation at 900 and 1000 °C for 25 h. The oxides of $CrTaO_4$ and $CrNbO_4$ disappear as the oxidation temperature elevated to 1100 °C.

I. INTRODUCTION

High-entropy alloys (HEAs), a new alloying concept, which originally proposed by Yeh et al.[1–4] According to this experimentally supported concept, the high entropy of mixed different metallic elements (generally ≥5) with near equimolar concentrations can considerably decrease the Gibbs free energy and stabilize disordered solid solution phases with relatively simple crystal structures rather than forming the conventionally expected complex intermetallic phases. Since proposed, a number of HEAs have attracted extensive research attention for both functional and structural applications due to the simple phase composition and excellent properties, which mainly consist of face-centered cubic (FCC) and/or body-centered cubic (BCC) crystal structures. So, HEAs have demonstrated favorable combinations of microhardness, strength, ductility, oxidation resistance, thermal stability, and corrosion resistance.[5–11] Among all these investigated HEA systems, the microstructures and properties of HEA systems with elements, such as Al, Cu, Co, Cr, Fe, Mn, Ni, Ti, and V, have been widely studied.[2–4,6,8,10–14]

Recently, to develop new alloys for elevated-temperature applications in advanced gas turbines or airplane engines, intensive research efforts have been devoted to refractory HEAs based on refractory elements such as Ta, Mo, W, Nb, Hf, Ti, V, and Zr. To the authors' knowledge, the concept of refractory HEAs is proposed by Senkov et al. at 2010.[15] Since then, more and more researchers began to study and investigate refractory HEAs. A series of refractory HEAs are reported, which show very encouraging properties. For example, the TaNbHfZrTi alloy has high compression yield strength ($\sigma_{0.2}$ = 929 MPa) and very high ductility ($\varepsilon > 50\%$),[16] the MoTaWNbV alloy has high microhardness ($HV_{0.5}$ = 7576 ± 201 MPa) and shows good wear resistance,[17] and other refractory HEAs such as NbTiVZr, CrNbTiZr, X–NbTaTiZr (X = Al, V, Cr, and Sn), HfNbTaTiZr, and $HfNbTiVSi_{0.5}$ also exhibit great properties.[18–21] These refractory HEAs consist of single BCC solid solution phase and are proved to be usable at high temperatures due to their high strength, but the oxidation

[a]Address all correspondence to this author.
e-mail: yioffice123@126.com
DOI: 10.1557/jmr.2018.340

 © Materials Research Society 2018

https://doi.org/10.1557/jmr.2018.340 Published online by Cambridge University Press

studies on the HEAs or equimolar alloys are not been extensively investigated.[9,22]

Based on the analysis above, a new refractory HEA CrMoNbTaV has been prepared in this work. The purpose of the present paper is to analyze the microstructure, microhardness, and high temperature oxidation behavior of the equiatomic CrMoNbTaV HEA.

II. EXPERIMENTAL PROCEDURE

The CrMoNbTaV HEA is prepared by vacuum arc melting in a water-cooled copper crucible under a Ti-gettered high-purity argon atmosphere. To synthesize the CrMoNbTaV HEA, first high-purity Cr, Mo, Nb, Ta, and V are compacted before being arc-melted. The purities of raw elemental materials Cr, Mo, Nb, Ta, and V are 99.7%, 99.95%, 99.95%, 99.95%, and 99.7%, respectively. The prepared buttons are flipped over and remelted at least four times to ensure the compositional homogeneity. X-ray diffraction (XRD) analysis is carried out on a Rigaku D/max2550VB diffractometer (Rigaku, Tokyo, Japan) with Cu K_α radiation and graphite monochromator operated at 40 kV. The diffraction peaks are identified using MDI Jade 6.0 software (Materials Data, Inc., Livermore, California). The microstructure and composition analysis are investigated by means of a scanning electron microscope (SEM; JSM-6360LV, JEOL, Tokyo, Japan) in the backscattered electron (BSE) mode equipped with an energy-dispersive X-ray spectroscope (EDS). The microhardness of the CrMoNbTaV HEA is measured on polished cross-sectional surfaces using a Vickers diamond pyramid under 9.807 N load applied for 15 s. For the oxidation tests, samples with dimension approximately 4 mm × 4 mm × 3 mm are cut from as-cast bars. They are ground to 1000 grit and polished in distilled water, then ultrasonically cleaned in ethanol to remove any dirt and grease. These samples are dried by electrothermal air blow drying cabinet before the tests. Isothermal oxidation tests of the samples are carried out at different temperatures (900, 1000, and 1100 °C) in air with the exposure times of 5 h, 10 h, 15 h, 20 h, and 25 h, respectively. Before and after oxidation experiments, the weight of the samples is examined and recorded by using an electronic balance with 0.0001 g sensitivity. The morphology and composition of oxidation products is analyzed by using the same experimental techniques as mentioned above. The cross section of the oxide scales is observed and analyzed by SEM.

III. RESULTS AND DISCUSSION

Figure 1(a) shows the XRD pattern of the as-cast CrMoNbTaV HEA. According to the XRD pattern analysis, it reveals four sharp diffracted peaks at 2θ = 39.7°, 57.5°, 72.2°, and 85.2°, which corresponded to the reflection planes of (110), (200), (211), and (220), respectively. This observation confirms that the as-cast alloy has a single BCC structure like many other refractory HEAs such as, $HfNbTiVSi_{0.5}$,[21] TiZrHfNbTa,[23] $Mo_{0.5}NbHf_{0.5}ZrTi$,[24] and MoNbHfZrTi.[25] And the lattice constant of the BCC structure is 0.320 nm. Back scattered-electron (BSE) SEM images of the as-cast alloy are presented in Figs. 1(b) and 1(c). It can be seen that the dendritic microstructure is obviously formed in the CrMoNbTaV alloy, which is typical of as-cast ingots. The dendrite arms appear to be more brighter (in terms of SEM image contrast) than the interdendritic regions. The dendrites are slightly rounded and rather branched in shape. The EDS analysis results show that the dendrite region is enriched in Mo and Ta elements with relatively higher melting points. By contrast, the interdendritic region is enriched in Cr and V elements which have lower melting points. The distribution of the Nb element with moderate melting point between dendrite and interdendritic is relatively uniform.

Based on the previous studies,[26–29] there are five parameters in formulating thermodynamic rules for the formation of the HEA phase: the atomic radius difference (δ), the mixing enthalpy (ΔH_{mix}), the mixing entropy (ΔS_{mix}), the electronegativity difference ($\Delta\chi$), and the valence electron concentration (VEC). They are defined by Eqs. (1)–(5), respectively.

$$\delta = 100\sqrt{\sum_{i=1}^{n} c_i(1 - r_i/\bar{r})^2}, \quad \bar{r} = \sum_{i=1}^{n} c_i r_i \quad , \qquad (1)$$

where, c_i is the at.% of the ith element, r_i is the atomic radius of the ith element, $\bar{r}$ is the average atomic radius of all the alloying elements in the present system, and n is the number of components. The numerical factor 100 is used to amplify the data for clarity; and

$$\Delta H_{\mathrm{mix}} = \sum_{i=1, i\neq j}^{n} \Omega_{ij} c_i c_j, \quad \Omega_{ij} = 4\Delta H_{\mathrm{mix}}^{\mathrm{AB}} \quad , \qquad (2)$$

where $\Delta H_{\mathrm{mix}}^{\mathrm{AB}}$ is the mixing enthalpy of binary AB atomic pairs; and

$$\Delta S_{\mathrm{mix}} = -R\sum_{i=1}^{n} c_i \ln c_i \quad , \qquad (3)$$

where R is the universal gas constant; and

$$\Delta\chi = \sqrt{\sum_{i=1}^{n} c_i(\chi_i - \bar{\chi})^2}, \quad \bar{\chi} = \sum_{i=1}^{n} c_i\chi_i \quad , \qquad (4)$$

where χ_i is the Pauling electronegativity of ith element and $\bar{\chi}$ is the average Pauling electronegativity of all the alloying elements in the present system; and

https://doi.org/10.1557/jmr.2018.340 Published online by Cambridge University Press

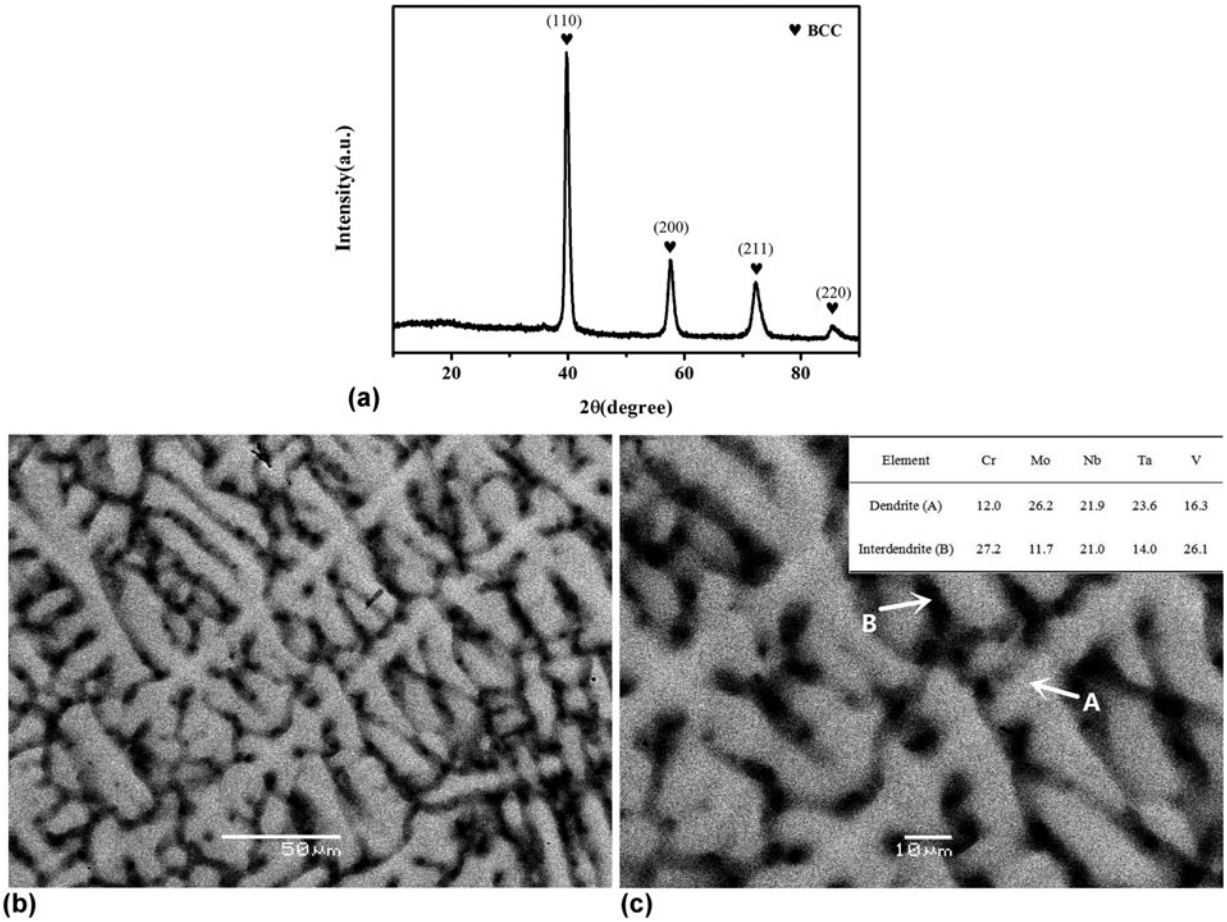


FIG. 1. XRD pattern (a) and BSE SEM images of the as-cast HEA CrMoNbTaV: (b) low magnification SEM image and (c) high magnification SEM image with EDS analysis results (at.%).

$$\mathrm{VEC} = \sum_{i=1}^{n} c_i (\mathrm{VEC})_i \quad , \tag{5}$$

where $(\mathrm{VEC})_i$ is the valence electron concentration of ith element.

The at.% (c_i), the atomic radius (r_i), the Pauling electronegativity (χ_i), and the valence electron concentration [$(\mathrm{VEC})_i$] of each element are exhibited in Table I. Meanwhile, as shown in Table II, the chemical mixing enthalpy $\left(\Delta H_{\mathrm{mix}}^{\mathrm{AB}}\right)$ of the binary equiatomic alloy was calculated based on Miedema's model proposed by Sun et al.,[30] to calculate the thermodynamic parameters for the present system. According to Eqs. (1)–(5), the thermodynamic parameters of the CrMoNbTaV HEA are calculated in Table III.

Guo et al.[27] showed that solid solution phases only form when the three parameters, δ, ΔH_{mix}, and ΔS_{mix}, are satisfying these criteria: $0 \le \delta \le 8.5$, $-22 \le \Delta H_{\mathrm{mix}} \le 7$ kJ/mol and $11 \le \Delta S_{\mathrm{mix}} \le 19.5$ J/(K mol), respectively. In this study, the calculated values of δ (6.95), ΔH_{mix} (−4.64 kJ/mol), and ΔS_{mix} [13.38 J/(K mol)] are well within the criteria. Guo et al.[27] also found that the valence electron concentration (VEC) plays a decisive role in determining the FCC- or BCC-type solid solution in

TABLE I. The at.%, the atomic radius, the Pauling electronegativity, and the VEC of each element in HEA CrMoNbTaV.

Element	Atomic percentage (c)	Atomic radius (r)/Å	Electronegativity (χ)[27]	VEC[28]
Cr	0.2	1.249	1.66	6
Mo	0.2	1.363	2.16	6
Nb	0.2	1.429	1.60	5
Ta	0.2	1.480	1.50	5
V	0.2	1.316	1.63	5

TABLE II. The chemical mixing enthalpy $\left(\Delta H_{\mathrm{mix}}^{\mathrm{AB}}\right)$ of binary equiatomic alloys calculated by Miedema's approach.

$\Delta H_{\mathrm{mix}}^{\mathrm{AB}}$ (kJ/mol)	Mo	Nb	Ta	V
Cr	0	−7	−7	−2
Mo	...	−6	−5	0
Nb	...	...	0	−1
Ta	...	...	...	−1

https://doi.org/10.1557/jmr.2018.340 Published online by Cambridge University Press

HEAs, and specially larger VEC (≥8) favors the formation of FCC-type solid solutions, while smaller VEC (≤6.87) favors the formation of BCC-type solid solutions. FCC and BCC coexist when VEC is larger than 6.87 and less than 8. The value of VEC is 5.4 in the present work, which indicates that BCC solid solution could exist steadily in our synthesized alloy, agreeing with the experimental results.

However, Guo et al.[27] thought that $\Delta\chi$ almost does not have an effect on the formation of the solid solution phase. But Singh et al.[29] found that $\Delta\chi$ is also an important factor in predicting solid solution formation; when $\Delta\chi \geq 10\%$, compound phases are also likely to form along with HEA solid solution. In this study, $\Delta\chi$ is calculated to be 23.13%; however, reflections of BCC single solid solution without compound phase are identified for the as-cast CrMoNbTaV HEA [Fig. 1(a)]. This result is well consistent with the criteria for the formation of solid solution of Guo et al.[27]

Microhardness measurements should provide first insight into the mechanical properties of the alloy at room temperature,[31] carried out on the as-cast sample. As expected, the interdendric regions show higher microhardness values compared to the dendrite areas. As shown in Fig. 2, the average microhardness value of the interdendritic regions is about 950 HV, while the corresponding value for the dendrite regions is about 896 HV. It may be caused by the content of element Cr, which in the interdendritic regions is higher than that in the dendrites regions. Compared to other HEAs such as TaNbHfZrTi (390 HV),[16] AlCrFeNiMo$_{0.2}$ (465 HV),[32] and NbCrMo$_{0.5}$Ta$_{0.5}$TiZr (539 HV),[33] the microhardness value of this alloy is much higher for the reason of the large difference of the atomic radius between the element Cr and other four elements. This difference makes the alloy has more significant lattice distortion effect, which strengthens the alloy so as to improve the microhardness. The microhardness indentation carried out on the as-cast sample clearly demonstrates the ductile nature of the alloy since cracks are neither detected in the dendrites nor in the interdendritic regions.

TABLE III. Calculated parameters δ, ΔH_{mix}, ΔS_{mix}, $\Delta\chi$, and VEC for CrMoNbTaV HEA.

Parameters	δ	ΔH_{mix} (kJ/mol)	ΔS_{mix} [J/(K mol)]	$\Delta\chi$/%	VEC
Value	6.95	−4.64	13.38	23.13	5.4

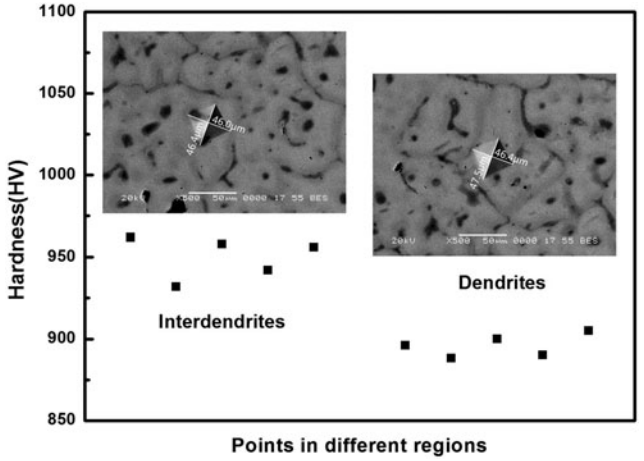


FIG. 2. The microhardness values and SEM images of dendrite and interdendrite regions of the as-cast HEA CrMoNbTaV.

Figure 3 shows thermogravimetric curves of the CrMoNbTaV HEA in the as-cast condition during exposure to laboratory air at 900, 1000, and 1100 °C. The oxidation kinetic curves at 900 and 1000 °C show the same tendency that the mass gain increases as the exposure time extends. The oxidation kinetic curves obtained at 900 and 1000 °C obey pseudo-parabolic rate law indicating that the growth of the oxide scale proceeds through solid state diffusion. And the oxidation rate at 1000 °C is substantially higher than that at 900 °C, and it reveals that the oxide scales belong to the nonprotective oxide scales.

To understand whether a simple kinetics law can apply, the curves can be fitted by an equation model[34] as

$$\Delta M_n = k_n t \quad , \tag{6}$$

where ΔM_n is the mass grain per unit surface area of the specimen, t is the exposure time, and k_n is the rate constant. The rate constant k_n and exponent n were evaluated from the linear regression fitting of ln(ΔM) versus ln t data. And the relationship[34] of the two data is as follows:

$$\ln(\Delta M) = \frac{1}{n}\ln t + \frac{1}{n}\ln k_n \quad . \tag{7}$$

And after taking logarithm of mass gain and exposure time, the oxidation kinetic curves of this alloy at 900 and

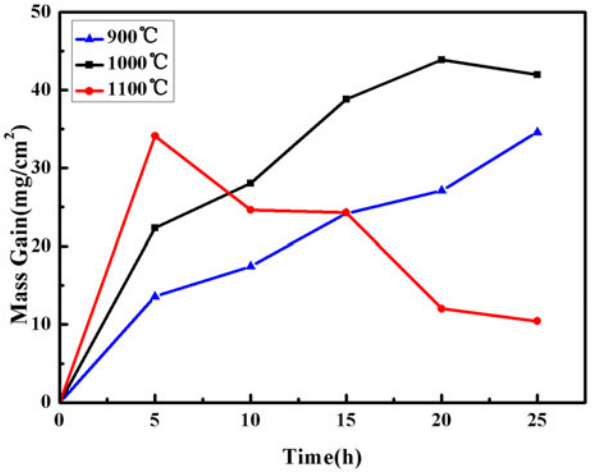


FIG. 3. Oxidation kinetics curves of the HEA CrMoNbTaV.

https://doi.org/10.1557/jmr.2018.340 Published online by Cambridge University Press

1000 °C obey pseudo-parabolic growth kinetics, and the values of n of this alloy after oxidation at 900 and 1000 °C for 25 h are 0.95 and 1.00, respectively. However, the thermogravimetric curve for 1100 °C shows a different tendency compared to that at 900 and 1000 °C. With the exposure time increasing, the mass change is found to increase first at 5 h, followed by continuous reduction. This may result from the fact that the oxide scale of this alloy after 1100 °C oxidation is likely to be detached from the matrix with the oxidation time increasing. It is proved that the oxidation behavior of this alloy is greatly influenced by the oxidation temperature.

Figure 4 presents the surface morphologies of the oxides after oxidation at 900, 1000, and 1100 °C for 25 h. The SEM micrographs reveal that a thick and continuous oxide-rich region is formed on the surface of this alloy, and the morphologies of the oxides formed at 900, 1000, and 1100 °C are similar. After oxidation at these three temperatures, long rod-shaped oxidation products are observed on alloy surface. It can be seen that the size of long rod-shaped oxidation products at 1100 °C is

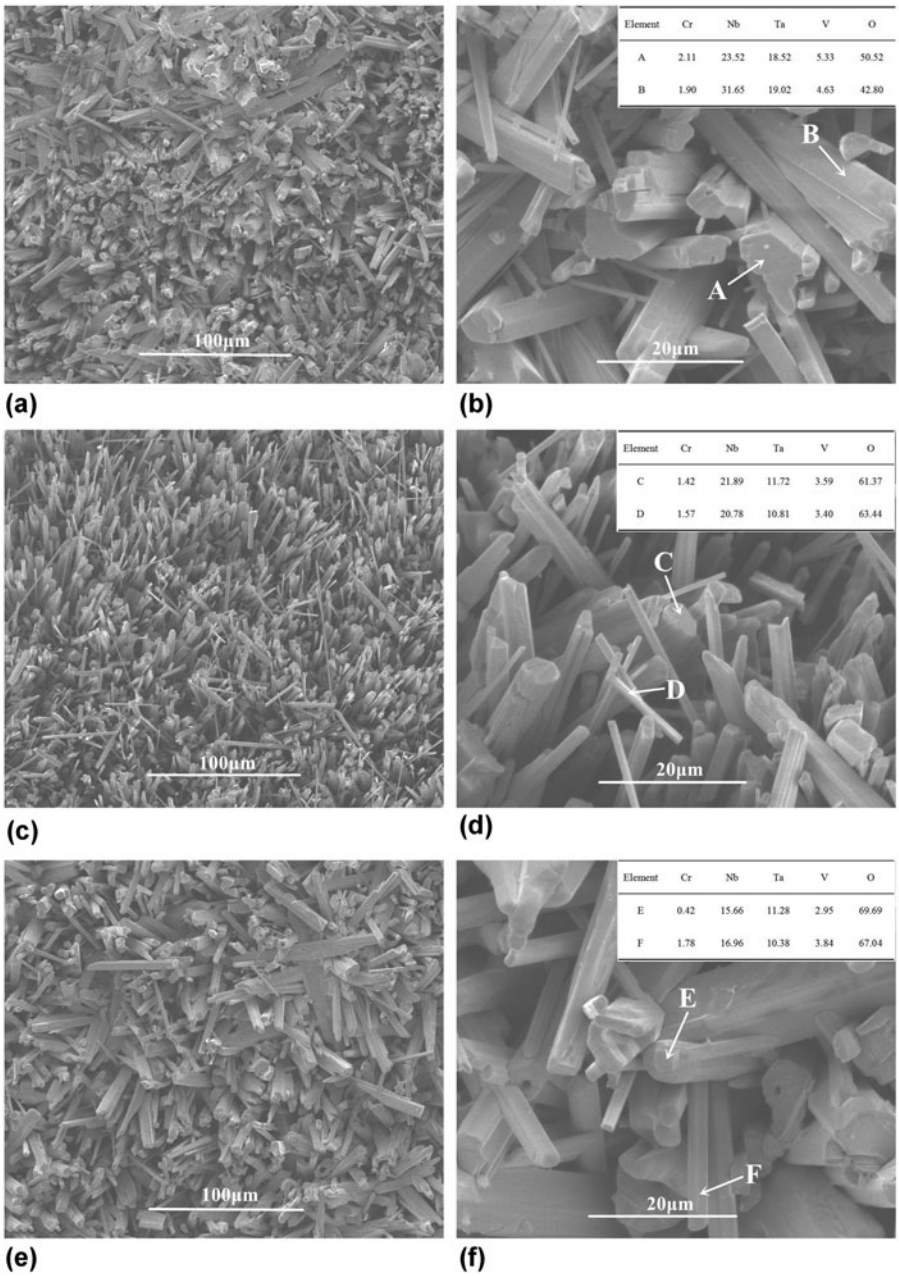


FIG. 4. BSE SEM images and EDS analysis results (at.%) of the surface morphologies after oxidation at (a and b) 900 °C, (c and d) 1000 °C, (e and f) 1100 °C.

https://doi.org/10.1557/jmr.2018.340 Published online by Cambridge University Press

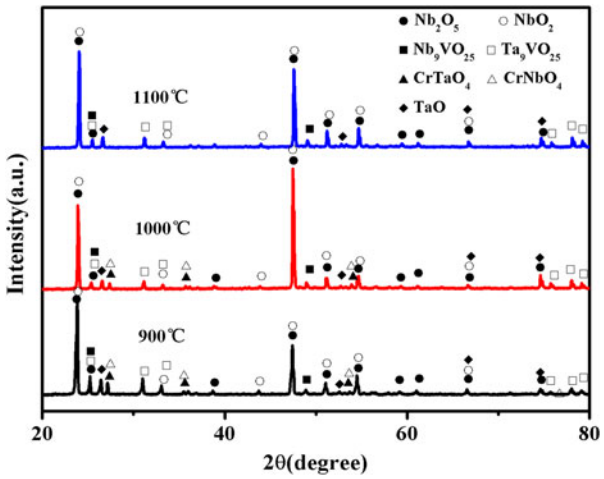


FIG. 5. XRD pattern of the CrMoNbTaV HEA after oxidation for 25 h.

somewhat larger than those of 900 and 1000 °C. One can note that all the oxidation products at these three temperatures show a trend of directional growth. The different oxides that are observed by the energy spectra analysis are marked in Figs. 4(b), 4(d), and 4(f). The EDS results show that most of the oxides are rich in Ta, Nb, and V. With the oxidation temperature increasing, the content of O increases gradually while the contents of Nb, Ta, and V decrease.

Figure 5 shows the XRD results of the surface oxides of this alloy after oxidation at 900, 1000, and 1100 °C for 25 h. It can be noted that the oxidation products formed on the alloy surfaces are similar at 900 and 1000 °C, being mainly Nb_2O_5, NbO_2, $CrTaO_4$, $CrNbO_4$, Ta_9VO_{25}, Nb_9VO_{25}, and TaO. As the oxidation temperature is elevated to 1100 °C, it can be seen clearly that all the peaks of $CrTaO_4$ and $CrNbO_4$ disappeared. The

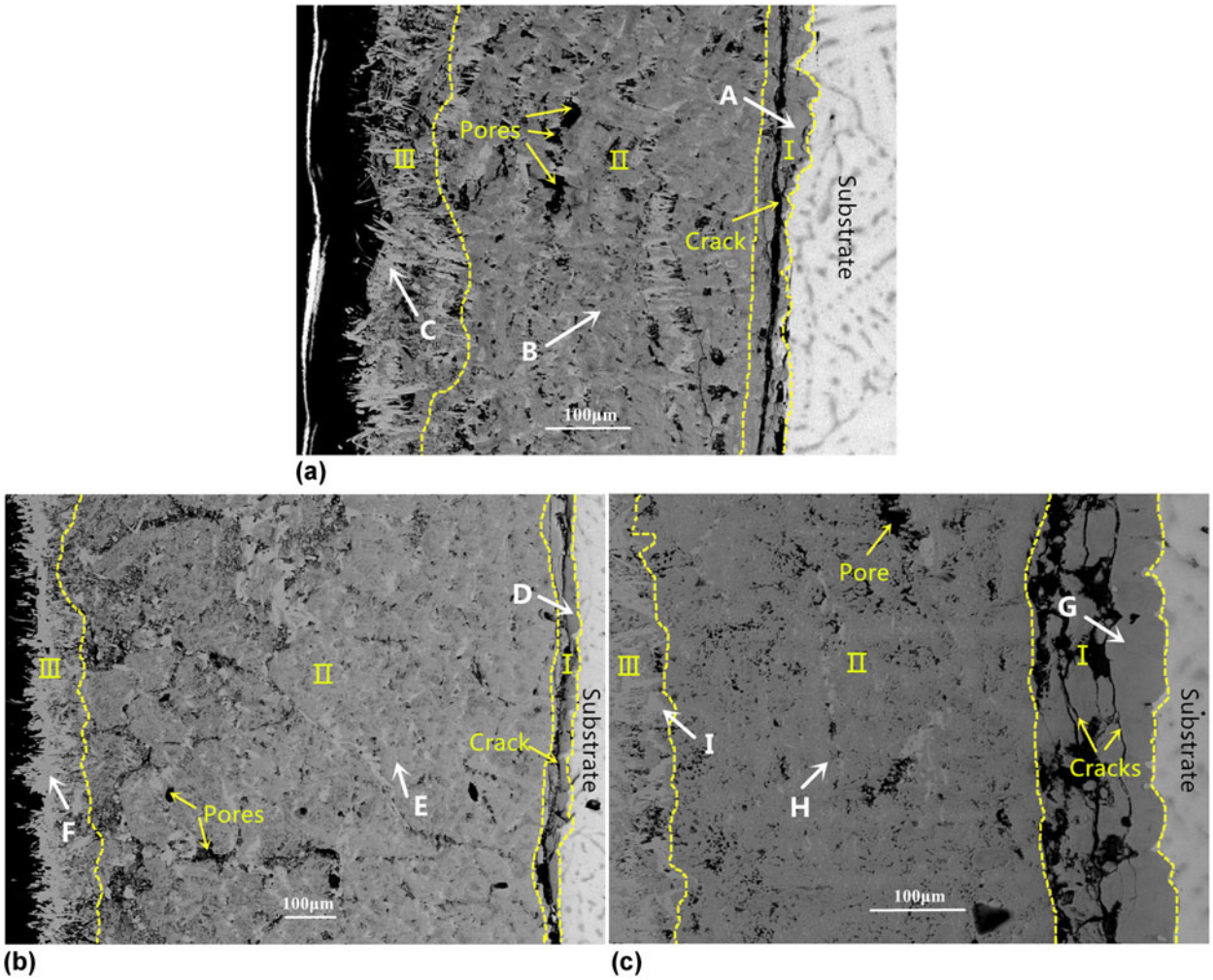


FIG. 6. BSE cross-sectional micrographs of the scales formed on the CrMoNbTaV HEA oxidized for 25 h at (a) 900 °C, (b) 1000 °C, and (c) at 1100 °C.

https://doi.org/10.1557/jmr.2018.340 Published online by Cambridge University Press

TABLE IV. Quantitative EDS chemical analyses (at.%) of the oxidation products indicated in Fig. 6.

Element	Cr	Mo	Nb	Ta	V	O
A	17.89	10.98	13.93	16.61	11.65	28.94
B	12.46	...	10.43	11.65	8.74	56.73
C	...	...	15.77	12.42	6.50	65.31
D	11.12	6.17	11.35	11.43	8.59	51.34
E	10.82	...	10.38	12.13	8.70	57.97
F	...	...	17.32	13.70	5.06	63.92
G	6.14	7.38	6.94	7.43	7.59	64.53
H	14.23	...	8.22	10.06	6.08	61.42
I	...	...	17.11	11.40	2.74	68.76

disappearance of $CrTaO_4$ and $CrNbO_4$ in the oxidation products at 1100 °C can be mainly attributed to the detachment of oxide scale from the matrix caused by oxidation temperature increasing.

To further investigate the oxide-rich region, the characteristics of cross sections are analyzed by SEM in Fig. 6 with corresponding EDS in Table IV. The images in Fig. 6 reveal that a thick and continuous oxide scale is formed on the surface of this alloy after oxidation at 900, 1000, and 1100 °C for 25 h. The thicknesses of oxide scales are measured to be about 530 μm, 1132 μm, and 600 μm at 900 °C, 1000 °C, and 1100 °C, respectively. From the pictures we can see that the morphologies of oxide scales at different oxidation temperatures are very similar. All the oxide scales can be divided into three regions: (I) a thin and attached to the substrate region, (II) a thick and porous oxide mixture, and (III) a relatively thin outer region. The innermost layer (region I), usually a diffusion layer, is thin and dense. A distinct crack is observed in the region I after oxidation at 900 and 1000 °C, while more cracks are formed in it as the oxidation temperature increased to 1100 °C. Region II with the largest thickness is composed of two microstructures, namely gray and white regions. In region II, more pores can be observed as compared with the case in regions I and III, indicating that the structure of oxide scale is looser. The outer oxide layer (region III) consists almost entirely of white phase. In addition, all the oxide scales at these three temperatures exhibit a slight tendency to flake.

The EDS analysis of the oxide scales in Table IV reveals that the scales consist of a mixture of Cr, Mo, Nb, Ta, and V oxides. The enrichment of Mo is only found at the interface oxide/substrate, which indicates that the evaporation of Mo oxides can be neglected.[9] According to the EDS analysis, the gray region in region II consists of a mixture of Cr, Nb, Ta, and V oxides, and the white region consists of a mixture of Nb, Ta, and V oxides. To sum up, the oxide scale consists of three regions: (I) a mixture of Cr, Mo, Nb, Ta, and V oxides, (II) a mixture of Cr, Nb, Ta, and V oxides, and (III) a mixture of Nb, Ta, and V oxides.

Based on the above results and discussion, the oxidation behavior of the CrMoNbTaV HEA can be summarized as follows. There is a thick and porous oxide layer formed on the surface of this alloy after oxidation at high temperature ranging from 900 °C to 1100 °C. This is mainly because that this alloy contains Mo and V elements, both of which have negative effects on the high-temperature oxidation behavior of the metallic material. The chemical stability of the Mo element is relatively lower, and Mo will react with O in the air when the temperature increases to 600 °C. The corresponding oxidation product MoO_3 is volatile with low melting point of 795 °C. The volatile process of MoO_3 can cause the structure of oxide scale loose and porous so that the alloy surface can not form a dense oxide thin layer. As a result, the alloy will have been "destructive" oxidation.[35] This is also the reason why there is no Mo element observed on the surface of the oxide layer. Adding too much V element will be adverse to the high temperature oxidation resistance of the alloy. This is because that V oxides including VO, VO_2, and V_2O_5 all have a low melting point and easy to volatilize at high temperature. With the oxidation temperature increasing, V oxides come out from the alloy oxide scale, which destroys the formation of the dense oxide layer.[36]

IV. CONCLUSIONS

In this paper, the microstructure, microhardness, and high temperature oxidation behavior of the equiatomic refractory HEA CrMoNbTaV are investigated. The main findings can be summarized as follows:

(1) The as-cast CrMoNbTaV HEA exhibits a dendritic microstructure with single BCC phase. The EDS analysis reveals that the dendrite region is enriched in Ta, Nb, and Mo, whereas the interdendritic region is enriched in Cr and V.

(2) The alloy has a very high microhardness value of 923 HV due to the strong solid solution strengthening effect. The average microhardness value in interdendrites (950 HV) was higher than that in dendrites (896 HV) because of composition segregation.

(3) The oxidation kinetic of the alloy after exposure to air at 900 and 1000 °C follows the pseudo-parabolic rate law, while the mass gain increases first and then decreases at 1100 °C. The metal surface is largely covered by thick, porous, and nonprotective oxide scales consisting of a mixture of various oxides. The thickness of the oxide layer increases with the increasing of oxidation time. The long rod-shaped oxidation products are composed of Nb_2O_5, NbO_2, $CrTaO_4$, $CrNbO_4$, Ta_9VO_{25}, Nb_9VO_{25}, and TaO after oxidation at 900 and 1000 °C for 25 h. The oxides of $CrTaO_4$ and $CrNbO_4$ disappear as the oxidation temperature is elevated to 1100 °C.

https://doi.org/10.1557/jmr.2018.340 Published online by Cambridge University Press

ACKNOWLEDGMENTS

This work was supported by the Hunan Provincial Natural Science Foundation of China (No. 2018JJ2395) and Project of Hunan Provincial Department of Education (No. 17A204).

REFERENCES

1. J.W. Yeh, S.K. Chen, S.J. Lin, J.Y. Gan, T.S. Chin, T.T. Shun, C.H. Tsau, and S.Y. Chang: Nanostructured high-entropy alloys with multiple principal elements: Novel alloy design concepts and outcomes. *Adv. Eng. Mater.* **6**, 299 (2004).
2. J.W. Yeh, S.J. Lin, T.S. Chin, J.Y. Gan, S.K. Chen, T.T. Shun, C.H. Tsau, and S.Y. Chou: Formation of simple crystal structures in Cu–Co–Ni–Cr–Al–Fe–Ti–V alloys with multiprincipal metallic elements. *Metall. Mater. Trans. A* **35**, 2533 (2004).
3. C.J. Tong, Y.L. Chen, J.W. Yeh, S.J. Lin, S.K. Chen, T.T. Shun, C.H. Tsau, and S.Y. Chang: Microstructure characterization of Al_xCoCrCuFeNi high-entropy alloy system with multiprincipal elements. *Metall. Mater. Trans. A* **36**, 881 (2005).
4. J.W. Yeh, S.Y. Chang, Y.D. Hong, P.H. Lee, and S.J. Lin: Anomalous decrease in X-ray diffraction intensities of Cu–Ni–Al–Co–Cr–Fe–Si alloy systems with multi-principal elements. *Mater. Chem. Phys.* **103**, 41 (2007).
5. Y. Deng, C.C. Tasan, K.G. Pradeep, H. Springer, A. Kostka, and D. Raabe: Design of a twinning-induced plasticity high entropy alloy. *Acta Mater.* **94**, 124 (2015).
6. Z. Wang, M.C. Gao, S.G. Ma, H.J. Yang, Z.H. Wang, M. Ziomek-Moroz, and J.W. Qiao: Effect of cold rolling on the microstructure and mechanical properties of $Al_{0.25}CoCrFe_{1.25}Ni_{1.25}$ high-entropy alloy. *Mater. Sci. Eng., A* **645**, 163 (2015).
7. C.C. Juan, M.H. Tsai, C.W. Tsai, C.M. Lin, W.R. Wang, C.C. Yang, S.K. Chen, S.J. Lin, and J.W. Yeh: Enhanced mechanical properties of HfMoTaTiZr and HfMoNbTaTiZr refractory high-entropy alloys. *Intermetallics* **62**, 76 (2015).
8. S.G. Ma, J.W. Qiao, Z.H. Wang, H.J. Yang, and Y. Zhang: Microstructural features and tensile behaviors of the $Al_{0.5}$CrCuFeNi$_2$ high-entropy alloys by cold rolling and subsequent annealing. *Mater. Des.* **88**, 1057 (2015).
9. B. Gorr, F. Mueller, H-J. Christ, T. Mueller, H. Chen, A. Kauffmann, and M. Heilmaier: High temperature oxidation behavior of an equimolar refractory metal-based alloy 20Nb–20Mo–20Cr–20Ti–20Al with and without Si addition. *J. Alloys Compd.* **688**, 468 (2016).
10. D.H. Xiao, P.F. Zhou, W.Q. Wu, H.Y. Diao, M.C. Gao, M. Song, and P.K. Liaw: Microstructure, mechanical and corrosion behaviors of AlCoCuFeNi–(Cr,Ti) high entropy alloys. *Mater. Des.* **116**, 438 (2017).
11. W. Zhang, P.K. Liaw, and Y. Zhang: Science and technology in high-entropy alloys. *Sci. China Mater.* **61**, 2 (2018).
12. C.W. Tsai, Y.L. Chen, M.H. Tsai, J.W. Yeh, T.T. Shun, and P.H. Lee: Deformation and annealing behaviors of high-entropy alloy $Al_{0.5}$CoCrCuFeNi. *J. Alloys Compd.* **486**, 427 (2009).
13. M.A. Hemphill, T. Yuan, G.Y. Wang, J.W. Yeh, C.W. Tsai, A. Chuang, and P. Liaw: Fatigue behavior of $Al_{0.5}$CoCrCuFeNi high entropy alloys. *Acta Mater.* **60**, 5723 (2012).
14. X. Chen, Y.W. Sui, J.Q. Qi, Y.Z. He, F.X. Wei, Q.K. Meng, and Z. Sun: Microstructure of $Al_{1.3}$CrFeNi eutectic high entropy alloy and oxidation behavior at 1000 °C. *J. Mater. Res.* **32**, 2109 (2017).
15. O.N. Senkov, G.B. Wilks, D.B. Miracle, C.P. Chuang, and P.K. Liaw: Refractory high-entropy alloys. *Intermetallics* **18**, 1758 (2010).
16. O.N. Senkov, J.M. Scott, S.V. Senkova, D.B. Miracle, and C.F. Woodward: Microstructure and room temperature properties of a high-entropy TaNbHfZrTi alloy. *J. Alloys Compd.* **509**, 6043 (2011).
17. A. Poulia, E. Georgatis, A. Lekatou, and A.E. Karantzalis: Microstructure and wear behavior of a refractory high entropy alloy. *Int. J. Refract. Met. Hard Mater.* **57**, 60 (2016).
18. O.N. Senkov, S.V. Senkova, C. Woodward, and D.B. Miracle: Low-density, refractory multi-principal element alloys of the Cr–Nb–Ti–V–Zr system: Microstructure and phase analysis. *Acta Mater.* **61**, 1545 (2013).
19. M.G. Poletti, S. Branz, G. Fiore, B.A. Szost, W.A. Crichton, and L. Battezzati: Equilibrium high entropy phases in X–NbTaTiZr (X = Al, V, Cr, and Sn) multiprincipal component alloys. *J. Alloys Compd.* **655**, 138 (2016).
20. W.Q. Wu, S. Ni, Y. Liu, and M. Song: Effects of cold rolling and subsequent annealing on the microstructure of a HfNbTaTiZr high-entropy alloy. *J. Mater. Res.* **31**, 3815 (2016).
21. Y. Zhang, Y. Liu, Y.X. Li, X. Chen, and H.W. Zhang: Microstructure and mechanical properties of a refractory HfNbTiV$Si_{0.5}$, high-entropy alloy composite. *Mater. Lett.* **174**, 82 (2016).
22. C.M. Liu, H.M. Wang, S.Q. Zhang, H.B. Tang, and A.L. Zhang: Microstructure and oxidation behavior of new refractory high entropy alloys. *J. Alloys Compd.* **583**, 162 (2014).
23. J-P. Couzinié, L. Lilensten, Y. Champion, G. Dirras, L. Perrière, and I. Guillot: On the room temperature deformation mechanisms of a TiZrHfNbTa refractory high-entropy alloy. *Mater. Sci. Eng., A* **645**, 255 (2015).
24. N.N. Guo, L. Wang, L.S. Luo, X.Z. Li, R.R. Chen, Y.Q. Su, J.J. Guo, and H.Z. Fu: Microstructure and mechanical properties of in situ MC-carbide particulates-reinforced refractory high-entropy $Mo_{0.5}$NbH$f_{0.5}$ZrTi matrix alloy composite. *Intermetallics* **69**, 74 (2016).
25. N.N. Guo, L. Wang, L.S. Luo, X.Z. Li, R.R. Chen, Y.Q. Su, J.J. Guo, and H.Z. Fu: Microstructure and mechanical properties of refractory MoNbHfZrTi high-entropy alloy. *Mater. Des.* **81**, 87 (2015).
26. S. Guo, Q. Hu, C. Ng, and C.T. Liu: More than entropy in high-entropy alloys: Forming solid solutions or amorphous phase. *Intermetallics* **41**, 96 (2013).
27. S. Guo and C.T. Liu: Phase stability in high entropy alloys: Formation of solid-solution phase or amorphous phase. *Prog. Nat. Sci.: Mater. Int.* **21**, 433 (2011).
28. http://www.webelements.com/.
29. A.K. Singh and A. Subramaniam: On the formation of disordered solid solutions in multi-component alloys. *J. Alloys Compd.* **587**, 113 (2014).
30. S.P. Sun, D.Q. Yi, H.Q. Liu, B. Zang, and Y. Jiang: Calculation of glass forming ranges in Al–Ni–RE (Ce, La, Y) ternary alloys and their sub-binaries based on Miedema's model. *J. Alloys Compd.* **506**, 377 (2010).
31. B. Gorr, M. Azim a, H-J. Christ, T. Mueller, D. Schliephake, and M. Heilmaier: Phase equilibria, microstructure, and high temperature oxidation resistance of novel refractory high-entropy alloys. *J. Alloys Compd.* **624**, 270 (2015).
32. Y. Dong, L. Jiang, H. Jiang, Y.P. Lu, T.M. Wang, and T.J. Li: Effects of annealing treatment on microstructure and hardness of bulk AlCrFeNiMo$_{0.2}$ eutectic high-entropy alloy. *Mater. Des.* **82**, 91 (2015).
33. O.N. Senkov and C.F. Woodward: Microstructure and properties of a refractory NbCr$Mo_{0.5}Ta_{0.5}$TiZr alloy. *Mater. Sci. Eng., A* **529**, 311 (2011).
34. J. Liu and X.Y. Xue: Isothermal oxidation behavior of TiAl–Nb–WBY alloys with different lamellar colony sizes. *Rare Met. Mater. Eng.* **45**, 1695 (2016).
35. Z.D. Li, G.Q. Zhang, Y.X. Zhao, and X.Y. Jia: Effects of alloying elements on high temperature oxidation resistance of Ni–Mo–Cr system superalloys. *Chin. J. Nonferrous Met.* **15**, 238 (2005).
36. D.B. Lee: Effect of Cr, Nb, Mn, V, W, and Si on high temperature oxidation of Ti Al alloys. *Met. Mater. Int.* **11**, 141 (2005).

https://doi.org/10.1557/jmr.2018.340 Published online by Cambridge University Press